

**Mohammad Al-Qahtani**

**Yong-Jun Jang**

Turbine Heat Transfer Laboratory,  
Department of Mechanical Engineering,  
Texas A&M University,  
College Station, TX 77843

**Hamn-Ching Chen**

Ocean Engineering Program,  
Department of Civil Engineering,  
Texas A&M University,  
College Station, TX 77843

**Je-Chin Han**

Turbine Heat Transfer Laboratory,  
Department of Mechanical Engineering,  
Texas A&M University,  
College Station, TX 77843

# Prediction of Flow and Heat Transfer in Rotating Two-Pass Rectangular Channels With 45-deg Rib Turbulators

*Numerical predictions of three-dimensional flow and heat transfer are presented for a rotating two-pass rectangular channel with 45-deg rib turbulators and channel aspect ratio of 2:1. The rib height-to-hydraulic diameter ratio ( $e/D_h$ ) is 0.094 and the rib-pitch-to-height ratio ( $P/e$ ) is 10. Two channel orientations are studied:  $\beta=90$  deg and 135 deg, corresponding to the mid-portion and the trailing edge regions of a turbine blade, respectively. The focus of this study is twofold; namely, to investigate the effect of the channel aspect ratio and the channel orientation on the nature of the flow and heat transfer enhancement. A multi-block Reynolds-averaged Navier-Stokes (RANS) method was employed in conjunction with a near-wall second-moment turbulence closure. In the present method, the convective transport equations for momentum, energy, and turbulence quantities are solved in curvilinear, body-fitted coordinates using the finite-analytic method. The numerical results compare reasonably well with experimental data for both stationary and rotating rectangular channels with rib turbulators at Reynolds number ( $Re$ ) of 10,000, rotation number ( $Ro$ ) of 0.11 and inlet coolant-to-wall density ratio ( $\Delta\rho/\rho$ ) of 0.115. [DOI: 10.1115/1.1450568]*

## Introduction

Modern gas turbine blades are designed to operate at increasingly higher inlet temperatures to improve thermal efficiency. To maintain acceptable blade life, sophisticated cooling techniques such as film cooling, impingement cooling and convective internal cooling are essential. Rotation of turbine blade cooling passages gives rise to Coriolis and buoyancy forces that can significantly alter the local heat transfer in the internal coolant passages due to the development of cross stream (Coriolis) as well as radial (buoyant) secondary flows. Moreover, the heat transfer augmentation is usually achieved by using repeated ribs as turbulence promoters. The presence of these ribs leads to further complex flow fields such as flow separation, reattachment and secondary flow between the ribs, which produces a high turbulence level that leads to high heat transfer coefficients. The complex coupling of the Coriolis and buoyancy forces with flow separation/reattachment by ribs has prompted many investigators to study the flow and temperature fields generated in heated, rotating ribbed wall passages. Experimental studies on rib-roughened channels have been quite extensive (see Han and Park [1]; Ekkad and Han, [2] (for non-rotating channels); and Wagner et al., [3]; Johnson et al. [4,5]; Parsons et al. [6]; and Zhang et al. [7], (for rotating square channels with normal and angled ribs). Dutta and Han [8] investigated the local heat transfer coefficients in rotating smooth and ribbed two-pass square channels with three channel orientations. They found that a change in the channel orientation about the rotating frame causes a change in the secondary flow structure and the associated flow and turbulence distribution. Consequently, the heat transfer coefficient from the individual surfaces changes. Parson et al. [6] studied the effects of the model orientation on the local heat transfer coefficients in a rotating two-pass square channel with ribbed walls. They found that the effect of the Coriolis force and cross-stream flow were reduced as the channel orienta-

tion changes from the 90 to 135-deg orientation. Recently, Azad et al. [9] studied the effect of the channel orientation ( $\beta=90$  and 135-deg from the direction of rotation) on two-pass rectangular channels for both smooth and 45-deg ribbed walls. For the smooth wall case, they found that the Nusselt number ratios for the first pass trailing and second pass leading surfaces with  $\beta=135$  deg are lower than those with  $\beta=90$  deg. Whereas, the Nusselt number ratios in the first pass leading and second pass trailing are higher compared to those with 90 deg. However, for the ribbed wall case, the channel orientation effect was less sensitive compared to the smooth wall case. Their study provided a data basis for the present work.

The earlier computational studies on internal coolant passages with ribs have mostly been restricted to two-dimensional flows (Liou et al. [10]). In recent years, a number of researchers have reported three-dimensional studies. Stephens et al. [11] and Rigby et al. [12], using a low-Reynolds number  $k-\omega$  turbulence model, presented the numerical simulations for flow and heat transfer in a nonrotating straight duct with normal 90-deg ribs. Stephens et al. [13] investigated flow and heat transfer characteristics in a straight non-rotating duct with angled, rounded ribs on two opposite walls and provided important characteristics on the angled rib ducts ( $k-\omega$  turbulence model). Stephens and Shih [14] and Shih et al. [15] investigated the effect of angled ribs on the heat transfer coefficients in a rotating two-passage duct using a low-Re number  $k-\omega$  turbulence model. They studied the effects of Reynolds numbers, rotation numbers, and buoyancy parameters. Their comparison with Johnson's et al. [4] data revealed that the heat transfer coefficient was underpredicted for the stationary case. However, the results for the rotating case were not clearly verified.

Prakash and Zerkle [16], employing a high Reynolds number  $k-\epsilon$  turbulence model with wall function, performed a numerical prediction of flow and heat transfer in a ribbed rectangular duct (90 deg rib) with and without rotation. However, their calculations used periodicity and neglected buoyancy effects. They suggested that a low Reynolds number model is necessary to simulate real gas turbine engine conditions and a Reynolds stress model is required to capture anisotropic effects. Bonhoff et al. [17] calculated

Contributed by the International Gas Turbine Institute and presented at the International Gas Turbine and Aeroengine Congress and Exhibition, New Orleans, Louisiana, June 4–7, 2001. Manuscript received by the IGTI, January 19, 2001. Paper No. 2001-GT-187. Review Chair: R. Natole.

the heat transfer coefficients and flow fields for rotating U-shaped coolant channels with angled ribs (45 deg). They used a Reynolds stress turbulence model with wall functions in the FLUENT CFD code. Their results show that the Nusselt number ratios of the rotating first pass leading and trailing surfaces are underpredicted compared to the experimental data. Using the periodicity of the flow, Iacovides [18] computed flow and temperature fields in a rotating straight duct with normal ribs. Two zonal models of turbulence were tested: a  $k-\varepsilon$  with a 1-equation model of  $k$  transport across the near-wall region and a low-Re differential stress model (DSM). He concluded that the DSM thermal computations were clearly superior to those of the  $k-\varepsilon$ /1-equation. Rigby et al. [19] presented numerical prediction of flow and heat transfer in a rotating ribbed (90 deg rib) coolant passage with a 180-deg turn. The computation was performed using a  $k-\omega$  turbulence model, and the heat transfer coefficient was overpredicted in the stationary case and underpredicted in the rotating case compared to experimental data. Iacovides and Raisee [20] explored turbulence modeling issues related to the computation of flow and heat transfer in internal cooling passages of turbine blades with normal ribs (90 deg). They tested four turbulence models: a zonal  $k-\varepsilon$ , a low-Re  $k-\varepsilon$ , a zonal differential stress model (DSM), and a low-Re DSM. They found that zonal models underpredicted surface heat transfer coefficients because they ignored the effects of transport on the near-wall turbulence scale. The low-Re closures were found to reproduce the correct surface heat transfer coefficients. In their results, the low-Re DSM model reproduced the turbulence field more reasonably than the  $k-\varepsilon$  model.

Chen et al. [21,22] studied rotating two-pass square channel with smooth walls. They used two turbulence models: a two-layer  $k-\varepsilon$  isotropic eddy viscosity model and a near-wall second-moment closure model. The near-wall second-moment closure model produced accurate predictions in comparison with Wagner et al. [23] data. Using the same model, Jang et al. [24,25] studied flow and heat transfer behavior in a non-rotating two-pass square channel with 60 deg and 90-deg ribs, respectively. Their results were in good agreement with Ekkad and Han's [2] detailed heat transfer data which validated their code and demonstrated the second-moment closure model superiority in predicting flow and heat transfer characteristics in the ribbed duct. In a later study, Jang et al. [26] predicted flow and heat transfer in a rotating square channel with 45-deg angled ribs by the same second-moment closure model. Heat transfer coefficient prediction was well matched with Johnson et al. [4] data for both stationary and rotating case. This has affirmed the superiority of the second-moment closure model compared to simpler isotropic eddy viscosity turbulence models. This model solves each individual Reynolds stress component directly from their respective transport equation. The primary advantage of this model is that it resolves the near-wall flow all the way to the solid wall rather than using log-law assumption in the viscous sublayer. With this near-wall closure, surface data like heat transfer coefficients and friction coefficients can be evaluated directly from velocity and temperature gradient on the solid wall. In view of the success achieved in the earlier studies, it is desirable to extend the present second moment RANS method to study more sophisticated cooling channel configurations. Most of the previous studies investigated coolant channels that have square cross sections and are perpendicular to the axis of rotation. However, the orientation of the cooling channel in the leading and trailing edge regions of the turbine blade may be at an angle  $\beta$  from the direction of rotation and its cross section may not be square. It is not well known how this affects the flow field and heat transfer characteristics. In the present study, numerical predictions of the three-dimensional flow and heat transfer are presented for the rotating two-pass rectangular duct (aspect ratio is 2:1) with 45-deg angled ribs and 180-deg sharp turn are presented. Meanwhile, this study investigates the effects of the channel orientation ( $\beta = 90$  and 135 deg) on the flow and heat transfer for the same geometry. In the present study, the

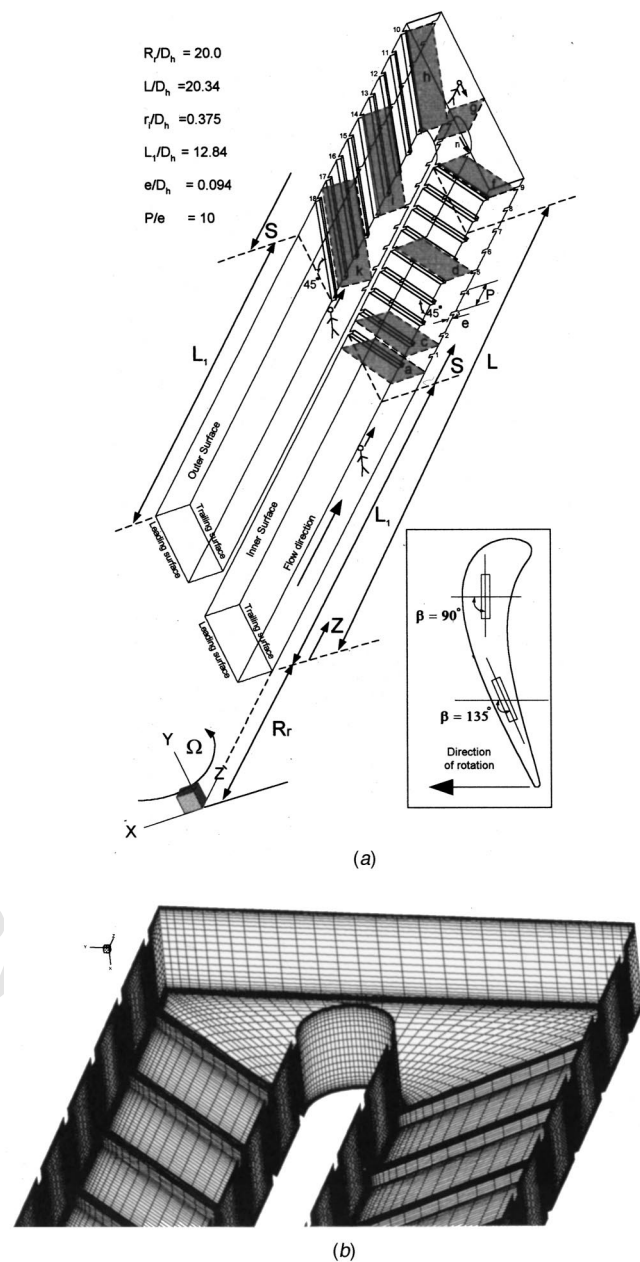


Fig. 1 (a) Geometry, (b) numerical grid

chimera RANS method of Chen et al. [21,22] was employed for the calculation of fluid flow and heat transfer in stationary and rotating ribbed channels. The numerical method and the governing equations of the turbulence model were described in detail by Chen et al. [21,22] and will not be repeated here.

### Description of Problem

Calculation was performed for the two-pass rectangular channel with 45-deg ribbed walls as tested by Azad et al. [9]. The geometry and numerical grids around the sharp 180-deg turn are shown in Fig. 1. The axial stations (at which results are presented) and the way to view them are also shown in Fig. 1. The geometry consists of a U-shaped channel of rectangular cross-section with channel aspect ratio of 2:1. The channel is made up of two straight passages and a 180 deg sharp turn. Two of the four side walls, in the rotational direction, are denoted as the leading and trailing surfaces, respectively, while the other two side walls are denoted

as the inner and outer surfaces. The channel hydraulic diameter,  $D_h$ , is 1.69 cm. The distance between the inlet of the duct and the axis of rotation ( $Y$ -axis) is given by  $R_r/D_h=20.0$ . The length of each of the first and second passages is given as  $L/D_h=20.34$ . Each passage consists of unheated smooth section and heated ribbed section. The length of the unheated smooth section is given by  $L_1/D_h=12.84$ . It extends from the inlet to the first rib in the first passage and from the exit to the last rib in the second passage. The arc length  $S$  is measured from the beginning of the ribbed section in the first passage (where heating starts) to the end of the ribbed section in the second passage (where heating ends). The radius of curvature of the 180 deg sharp turn is given as  $r_i/D_h=0.375$ . In the ribbed section, the leading and trailing surfaces for both the first and second passages are roughened with nine equally spaced ribs of square cross section. The rib height-to-hydraulic diameter ratio ( $e/D_h$ ) is 0.094 and the rib-pitch-to-height ratio ( $P/e$ ) is 10. All ribs are inclined at an angle  $\alpha=45$  deg with respect to the flow. Two channel orientations are studied:  $\beta=90$  deg corresponding to the mid-portion of a turbine blade and  $\beta=135$  deg corresponding to the serpentine passages in the trailing edge region of a blade. In this study, the Reynolds number ( $Re$ ) was fixed at 10,000. The inlet coolant-to-wall density ratio ( $\Delta\rho/\rho$ ) was fixed at 0.115. Three cases were studied: 1) nonrotating channel ( $Ro=0.0$ ), 2) rotating channel ( $Ro=0.11$ ) with channel orientation angle,  $\beta$ , of 90 deg and 3) rotating channel ( $Ro=0.11$ ) with channel orientation angle,  $\beta$ , of 135 deg.

A uniform velocity profile was used at the inlet of the duct ( $Z=0$ ). The unheated length ( $L_1$ ) was long enough for the velocity profile to be fully developed turbulent profile before the heating start-point ( $Z=L_1$ ). The flow was assumed to be parabolic at the exit of the duct (i.e. zero-gradient boundary conditions) for mean velocity and all turbulence quantities, while linear extrapolation was used for the pressure field. The coolant fluid at the inlet of the duct is air at uniform temperature  $T=T_o$  (i.e.,  $\theta=(T-T_o)/(T_w-T_o)=0$ ). The wall temperature of the smooth section is kept constant at  $T=T_o$  ( $\theta=0$ ) while the wall temperature of the ribbed section, including the ribs, is kept constant at  $T=T_w$  ( $\theta=1$ ).

The Nusselt numbers presented here were normalized with a smooth tube correlation by Dittus-Boelter/McAdams (Rohsenow and Choi [27]) for the fully developed turbulent flow in a smooth stationary pipe

$$Nu_o = 0.023 Re^{0.8} Pr^{0.4}$$

The present numerical grid was generated using an interactive gridding code GRIDGEN. It was divided into five-overlapped Chimera grid blocks to facilitate the implementation of the near-wall turbulence model and the specification of boundary conditions. To provide adequate resolutions of the viscous sublayer and buffer layer adjacent to a solid surface, the minimum grid spacing in the near-wall region is maintained at  $10^{-3}$  of the hydraulic diameter which corresponds to a wall coordinate  $y^+$  of the order of 0.5. In all calculations, the root-mean-square (rms) and the maximum absolute errors for both the mean flow and turbulence quantities were monitored for each computational block to ensure complete convergence of the numerical solutions. A convergence criterion of  $10^{-5}$  was used for the rms error.

The present grid uses  $33 \times 41 \times 804$  grid points (804 in the streamwise direction and  $33 \times 41$  in the cross-stream directions) with a total number of approximately 1,100,000 points. This choice is based on three systematic grid-refinement studies performed earlier for the prediction of flow and heat transfer in similar geometries. The geometry used in the first study (Jang et al. [25]) was a 90-deg ribbed two-pass square channel with nine ribs and a total grid points of 1,060,000 ( $Re=30,000$ ). In the second study (Jang et al. [24]), a total of 1,020,000 grid points was used for a 60-deg ribbed two-pass square channel with nine ribs ( $Re=30,000$ ). The total grid points in the third study (Jang et al. [26]) was 1,000,000 for a 45-deg ribbed one-pass square channel with 13 ribs ( $Re=25,000$ ). The numerical grids used in these

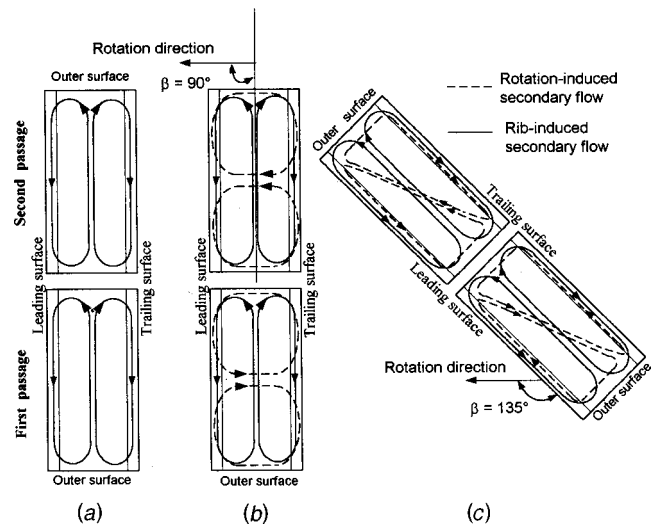


Fig. 2 Conceptual view of the secondary flow induced by angled ribs and rotation.

studies were shown to yield nearly grid-independent results. Also, their results were in close agreement with the experimental data. Note that the number of grid points used in the present rectangular configuration is comparable to the above mentioned geometries. In addition, the Reynolds number used in the present study ( $Re=10,000$ ) is lower than the one used in the previous studies. Therefore, it is believed that the present grid will produce nearly grid-independent results with accurate resolution of the boundary layer profile and Nusselt number distribution.

## Results

This section presents the three-dimensional mean flow and temperature fields for the rotating rectangular duct with 45-deg angled ribs. Computations were performed for non-rotating ( $Ro=0.0$ ) and rotating ( $Ro=0.11$ ) cases with two channel orientations of  $\beta=90$  and 135 deg at a Reynolds number of 10,000 and an inlet coolant-to-wall density ratio of 0.115.

**Velocity and Temperature Fields.** Before discussing the detailed computed velocity field, a general conceptual view about the secondary flow patterns induced by angled ribs and rotation is summarized and sketched in Fig. 2. The parallel angled ribs in the nonrotating duct (case 1, Fig. 2(a)) produce symmetric counter-rotating vortices that impinge on the inner surface in the first passage and on the outer surface in the second passage. The Coriolis force in the 90-deg rotating duct (case 2, Fig. 2(b)) produces two additional counter-rotating vortices that push the cooler fluid from the core to the trailing surface in the first passage, and to the leading surface in the second passage. For the 135-deg rotating duct (case 3, Fig. 2(c)), the Coriolis force produces secondary flow that migrates diagonally away from the corner of the inner-leading surfaces toward the center of the channel in the first passage, and from the corner of the inner-trailing surfaces towards the center of the channel in the second passage.

For a nonrotating duct (case 1), Fig. 3 is a plot of the secondary flow in the inter-rib regions on a plane parallel to the leading and trailing surfaces and  $1/10$  rib height away from any of them. The 45-deg inclined ribs in the first passage (Fig. 3(a)) induce fast secondary flow that moves parallel to the ribs from the inner surface (where it is strongest) to the outer surfaces (where it is weakest). The situation is reversed in the second passage (Fig. 3(b)). The ribs induce secondary flow from the outer surface (where it is strongest) to the inner surface (where it is weakest). Note that this secondary flow pattern is the same in all inter-rib areas. The consequence of this fast secondary flow is explained in Fig. 4.

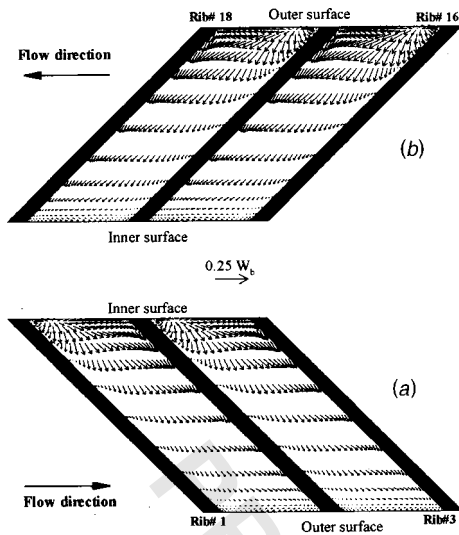


**Fig. 3 Velocity vectors 1/10 rib height from the leading and trailing surfaces for non-rotating case (plotted every other vector)**

Figure 4 is a plot of the calculated secondary flow vectors and constant temperature contours for the non-rotating case at several axial stations as shown in Figure 1. Figs. 4(a) through 4(f) (first passage) are viewed from upstream of the first passage, while Figures 4(g) through 4(l) (middle of the bend and second passage) are viewed from downstream of the second passage. The secondary flow field will be discussed first and then its effect on the temperature field. In the first passage, and as the fluid approaches the first rib (Fig. 4(a)), the rib induced fast secondary flow dis-

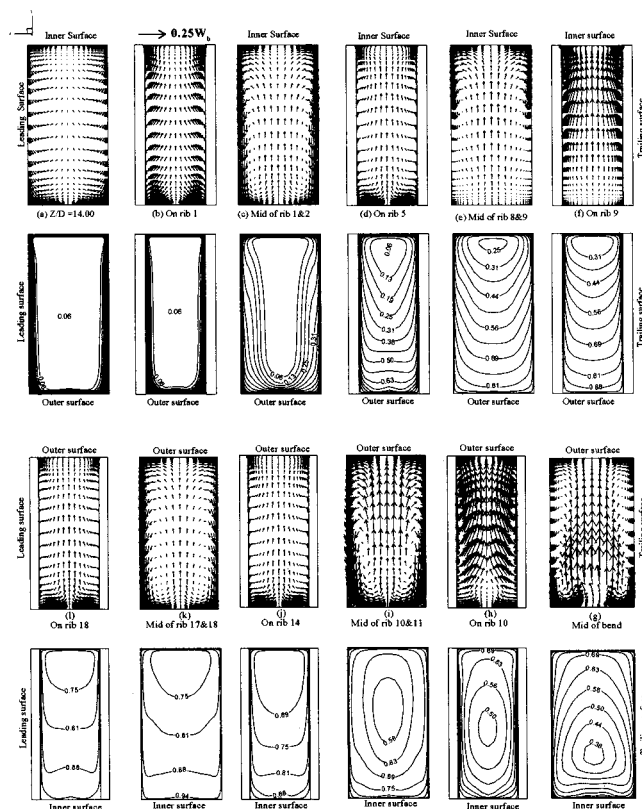


**Fig. 4 Secondary flow and temperature  $[\theta = (T - T_o)/(T_w - T_o)]$  for non-rotating duct,  $Ro=0.0$**

ussed in Fig. 3(a) moves towards the outer surface and returns back to the inner surface along the centerline of the inclined cross-stream plane. In the same figure, one can also notice the early stages of two symmetric counter-rotating vortices, which shrink in size on the first rib (Fig. 4(b)), and by the midsection of ribs 1 and 2 (Fig. 4(c)) become two full symmetric counter-rotating vortices. Along the streamwise direction, the size of these two vortices oscillate from the largest in the middle of each inter-rib distance to the smallest on the ribs (Fig. 4(d)). This pattern keeps repeating until rib 8. However, midway between ribs 8 and 9 (Fig. 4(e)) the strength of those two vortices shifts towards the inner surface. On rib 9 (Figure 4(f)), the secondary flow becomes a strong fluid motion from the outer to the inner surface due to the turn effects.

Upon entering the turn, the curvature induced secondary flow (which pushes fluid from the inner to outer surface) overcomes the rib induced secondary flow discussed in Figure 4(f), and the direction of the secondary flow is reversed and becomes from the inner to outer surface. This happens in less than one hydraulic diameter after the ninth rib. As the fluid proceeds towards the center of the turn, we notice the gradual formation of two counter-rotating vortices that reach their full size by the center of the turn (Fig. 4(g)). The size of these two vortices begin to decrease gradually as the fluid approaches the second sharp corner and soon is mixed with the second passage rib-induced secondary flow (Fig. 4(h)) resulting in a complex secondary flow. In the second passage and as discussed in Fig. 3(b), the rib induced fast flow is reversed in direction due to the opposite rib angle compared to the first passage. Here, Fig. 4(i) the rib induced secondary flow moves from the outer to the inner surfaces and returns back to the outer surface along the centerline of the inclined crossstream. As a result, two symmetric counter-rotating vortices are formed. The size of these two vortices oscillate in size from the smallest on each rib (Fig. 4(j)) to the largest in the midsection between each two ribs (Fig. 4(k)). This pattern keeps repeating until rib 18 (Fig. 4(l)). Due to the absence of the ribs, the secondary flow decreases gradually after rib 18 and vanishes almost completely  $7D_h$  after rib 18.

The overall effect of this secondary flow structure on the temperature field will be discussed here, referring to the temperature contour plots in Fig. 4. In the first passage, the effect of the secondary flow is convecting the cooler fluid from the inner surface and along the ribbed surfaces towards the outer surface. It then moves back to the inner surface which results in steep temperature gradients and high heat transfer coefficients on both the inner and ribbed surfaces as seen in the corresponding temperature contours. In the middle of the turn, the two counter-rotating vortices convect fluid from the core towards the outer surface, resulting in a steeper temperature gradient and thus a higher heat transfer coefficients on the outer surface. In the second passage, the secondary flow convects the cooler fluid from the outer surface and along the ribbed surfaces towards the inner surface. It then moves back to the outer surface resulting in steep temperature gradients and high heat transfer coefficients on both the outer and ribbed surfaces as seen in the corresponding temperature contours.

Figure 5 is a plot of the cross-stream velocity vectors and temperature contours for case 2 ( $Ro=0.11$  and  $\beta=90$  deg) at the same planes as in the non-rotating duct (case 1). A few hydraulic diameters before the first rib, the Coriolis force was found to produce two counter-rotating vortices that push the cooler fluid at the core towards the trailing surface and then returns along the inner and outer surfaces. As the flow approaches the first rib, this Coriolis force induced secondary flow starts to distort the secondary flow started by the inclined ribs. This effect can be clearly seen by comparing Figs. 5(a) through (f) with Figs. 4(c) through (f). From this comparison, the following conclusions can be drawn. The magnitude of the Coriolis force induced secondary flow is weaker than the rib induced secondary flow. In the mid-sections of each of two ribs, the rib induced vortex near the leading surface is weakened while the other vortex near the trailing

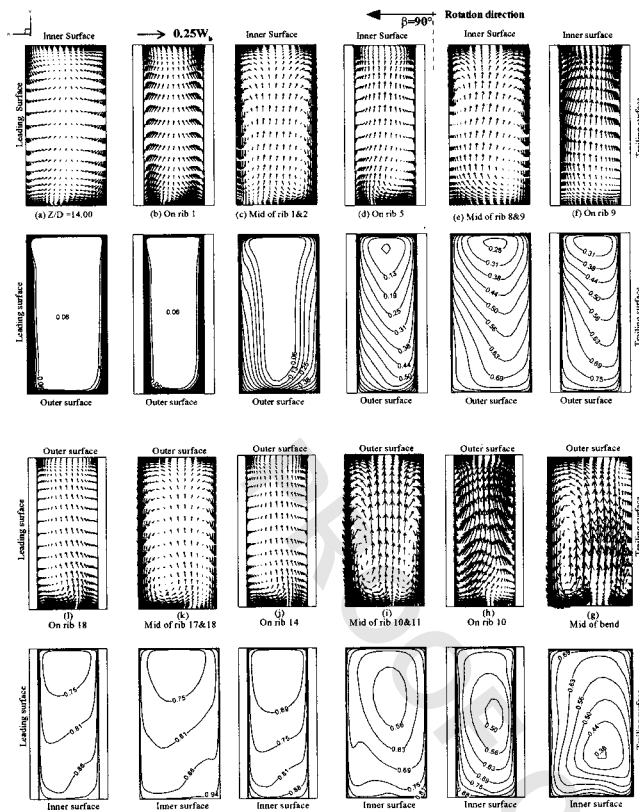


Fig. 5 Secondary flow and temperature  $[\theta=(T-T_o)/(T_w-T_o)]$  for rotating duct,  $Ro=0.11$  and  $\beta=90$  deg

surface is strengthened (Fig. 5(c)). This pattern repeats itself until midway between ribs 8 and 9 (Fig. 5(e)), where the larger vortex near the trailing surface grows at the expense of the smaller vortex near the leading surface, which shrinks in size and moves toward the inner surface. On the ribs (Fig. 5(d)), both vortices shrink in size and get distorted significantly by the Coriolis force induced secondary flow. This pattern repeats itself until rib 9, where the turn effect alters significantly the secondary flow structure, as seen in Fig. 5(f).

The general effect of the Coriolis force induced secondary flow in the first passage is to distort the rib induced vortices. Consequently, the temperature contours are shifted toward the trailing surface, which affects the heat transfer coefficients from both the leading and trailing surfaces as seen from the corresponding temperature contour plot. Notice that, in the turn (Fig. 5(g)), the vortex near the leading surface grew considerably at the expense of the one next to the trailing surface, which was weakened and split into two small vortices near the two corners of the trailing surface. This results in pushing the cold fluid toward the outer and trailing surfaces as seen in the corresponding contour plot. This effect dominates until rib 10 which is the first rib in the second passage (Fig. 5(h)). After rib 11, the Coriolis force induced secondary flow (which pushes the cold fluid towards the leading surface) gradually overcomes the turn induced secondary flow (which pushes the cold fluid toward the trailing surface). This is shown clearly in the temperature contour plots of Figs. 5(g) through (l).

Figure 6 is a plot of the cross-stream velocity vectors and temperature contours for case 3 ( $Ro=0.11$  and  $\beta=135$  deg) at the same planes as in the rotating case. The discussion of this figure is based on comparing Fig. 6 (case 3:  $Ro=0.11$  and  $\beta=135$  deg) and Fig. 5 (case 2:  $Ro=0.11$  and  $\beta=90$  deg). A few hydraulic diameters before the first rib, the Coriolis force produces secondary flow that migrates diagonally away from the corner of the inner-leading surfaces toward the center of the channel. As the

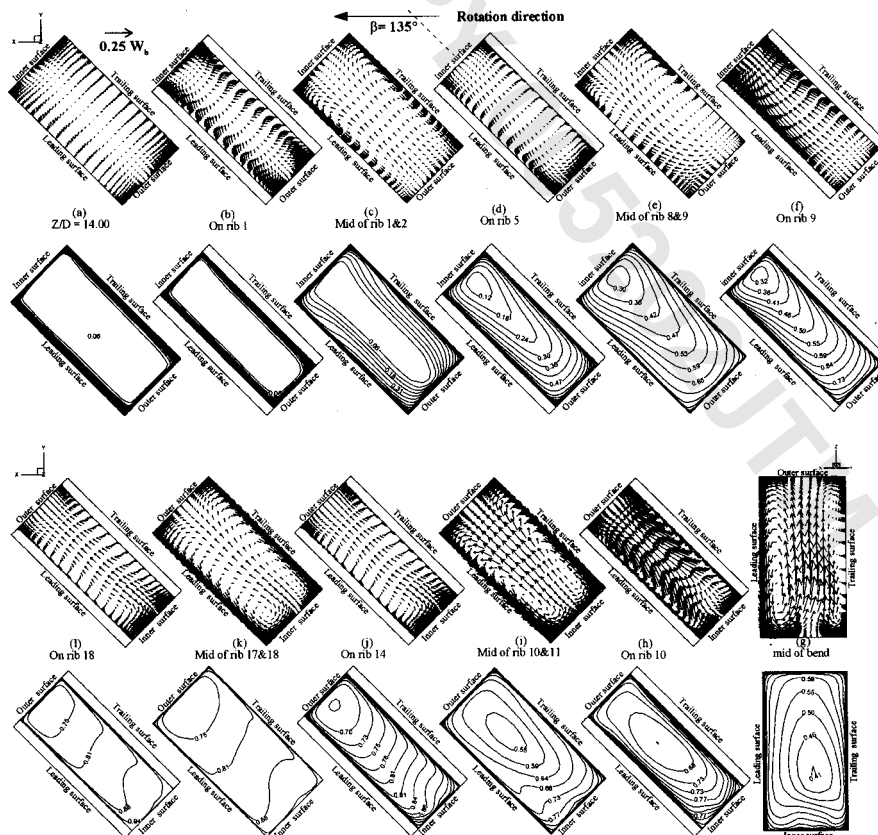
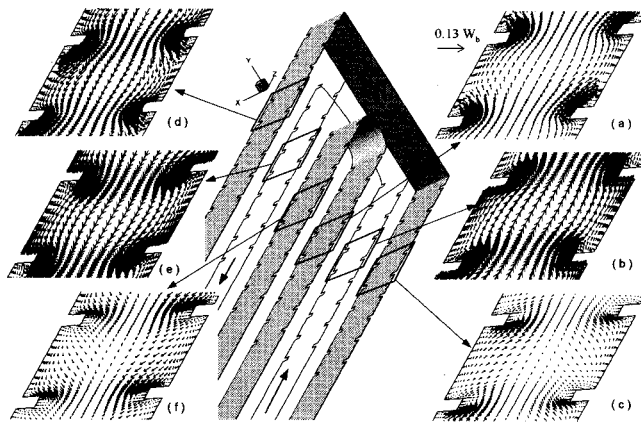


Fig. 6 Secondary flow and temperature  $[\theta=(T-T_o)/(T_w-T_o)]$  for rotating duct,  $Ro=0.11$  and  $\beta=135$  deg



**Fig. 7 Streamwise velocity vector distribution for non-rotating duct (case 1) at three planes:  $0.002D_h$  below the inner surface, midway between the inner and outer surfaces and  $0.002D_h$  above the outer surface**

flow approaches the first rib, this Coriolis force induced secondary flow distorts the secondary flow started by the inclined ribs. This effect can be clearly seen by comparing Fig. 6(a) with Fig. 5(a). However, from rib 1 on, this rotation induced secondary flow is dominated by the rib induced secondary flow. A careful comparison between the secondary flow fields of case 3 and case 2 (e.g., Fig. 6(d) with Fig. 5(d)) shows that the rotation induced secondary flow in case 3 ( $\beta = 135$  deg) changes the rib induced secondary flow compared to case 2 ( $\beta = 90$  deg). This change appears more clearly in the temperature field. By comparing the temperature contours in Fig. 6 ( $Ro = 0.11$  and  $\beta = 135$  deg) with Fig. 5 ( $Ro = 0.11$  and  $\beta = 90$  deg), we notice the following. In the first passage, the cooler fluid is pushed back toward the leading surface, reducing the steep temperature gradients on the trailing surface. The temperature contours do not change much in the bend (Fig. 6(g)). In the beginning of the second passage (Fig. 6(h)), the cooler fluid is pushed back slightly toward the leading surface, while the temperature field in the rest of the second passage is the same as in case 2.

Figure 7 is a plot of the streamwise velocity vector distribution for the nonrotating duct (case 1) at three planes:  $0.002D_h$  below the inner surface, midway between the inner and outer surfaces, and  $0.002D_h$  above the outer surface. A detailed investigation of the streamwise velocity field between the inner and outer surfaces revealed the following. In the first passage and near the inner surface (Fig. 7(a)), fairly large separation bubbles extend about 4 rib heights downstream of the rib followed by a reattachment region that separates once again about one rib height upstream of the next rib. The size of the separation bubble after the rib decreases as we move away from the inner surface (parallel to the rib), and no reattachment is found once we reach the mid plane between the inner and outer surfaces (Fig. 7(b)). Moving further toward the outer surface, the flow separation resumes occurring only on top of the rib (Fig. 7(c)). The flow is able to reattach near the inner surface because the secondary flow boundary layer in this region is very thin. As we move toward the outer surface, the secondary flow boundary layer gets thicker. Hence, the mainstream flow can not reattach in these regions. In the second passage, the large separation bubbles are formed near the outer surface (Fig. 7(d)). The separation region extends to about 3.79 rib heights after the rib, followed by a reattachment region that separates again about one rib height before the next rib. Moving towards the inner surface, the size of the separation bubble decreases until no reattachment is found midway between the outer and inner surfaces (Fig. 7(e)). Separation resumes upon approaching the inner surface (Fig. 7(f)) and occurs only on the rib top. Moreover, in the first passage, velocity magnitude near the inner

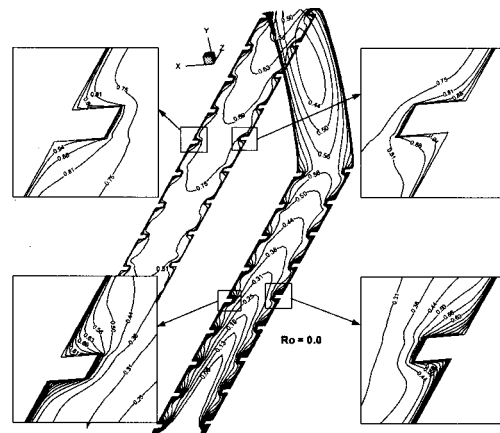


**Fig. 8 Temperature contours midway between the inner and outer surfaces for case 1 ( $Ro = 0.0$ )**

surface (Fig. 7(a)) is larger than the one near the outer surface (Fig. 7(a)). The reason is that the rib induced secondary flow near the inner surface is much stronger than the one near the outer surface. For the same reason mentioned above; the second passage velocity magnitude near the outer surface (Fig. 7(d)) is larger than the one near the inner surface (Fig. 7(f)). It should be mentioned that in this figure the apparent non-symmetric velocity field between the leading and trailing sides is a result of the angled 3-D view. This was confirmed by orthogonal 2-D views (not shown).

Figure 8 shows the temperature contours for the nonrotating case midway between the inner and outer surfaces for the whole duct. In the first passage, a thin thermal boundary layer forms first near the leading and trailing surfaces. However, the periodic ribs disturb and break the viscous sublayer and create high level of turbulence in the near-wall region. The steeper temperature gradients can be seen on the rib tip (due to flow impingement) and between the two adjacent ribs (due to flow reattachment), but the smaller temperature gradients are found right before and after the rib (due to a separation bubble). A much higher temperature exists in the second passage due to the thermal boundary layer thickening.

**Detailed Local Heat Transfer Coefficient Distribution.** Figure 9(a) is a plot of the local Nusselt number ratio contours on both the leading and trailing surfaces for the nonrotating case. The entrance and exit regions were cut to focus on the ribs and turn effects. The highest Nusselt number ratios were obtained on the top of the ribs, and the lower Nusselt number ratios were obtained right before and after the ribs for the first and second passages, respectively. Between any two ribs in the first passage, the Nusselt number ratios are highest near the inner surface and decrease as we move towards the outer surface. This is due to the rib induced secondary flow moving from the rib leading to the trailing side as shown in Fig. 3(a). Moreover, the Nusselt number ratios between the ribs increased gradually along the first passage until the flow approaches the seventh rib, where it decreases gradually until the ninth rib. Nusselt number ratios in the turn are higher in the region next to the divider wall tip while lower at the first corner. In the second passage (between any two ribs), the Nusselt number ratios are higher near the outer surface and decrease as we move toward the inner surface. Again, this is a result of the rib induced secondary flow in the second passage shown in Fig. 3(b).

Figures 9(b) and (c) show the Nusselt number ratio contours on the leading side for case 2 ( $Ro = 0.11$  and  $\beta = 90$  deg) and case 3 ( $Ro = 0.11$  and  $\beta = 135$  deg), respectively. Comparing these figures with the nonrotating leading side (Fig. 9(a)), we notice that the Nusselt number ratios decrease in the first passage, in both

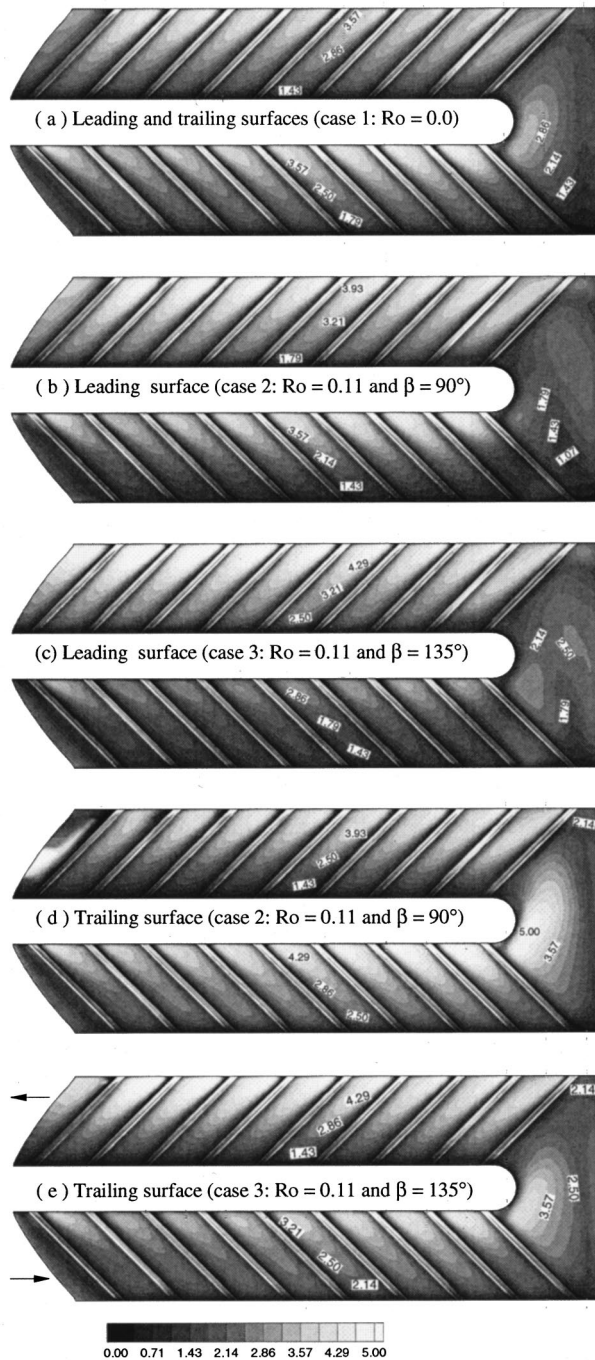


Fig. 9 Detailed Nusselt number ratio distribution

cases, with the decrease in case 3 being higher. In the second passage, the Nusselt number ratios in both cases increase with respect to case 1.

Figures 9(d) and (e) show the Nusselt number ratios contours on the trailing surface for case 2 ( $Ro=0.11$  and  $\beta=90$  deg) and case 3 ( $Ro=0.11$  and  $\beta=135$  deg), respectively. Comparing these figures with the non-rotating trailing side (Fig. 9(a)), we notice that the Nusselt number ratios increase in the first passage, for both cases, with the increase in case 2 being higher. In the second passage, the Nusselt number ratios in both cases decrease, with the decrease in case 2 being higher. The Nusselt number in the bend is much higher for both cases when compared to the non-rotating case.

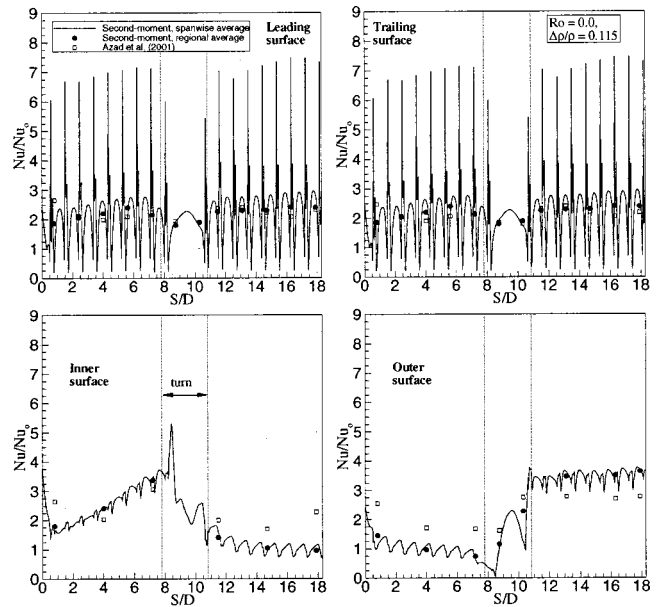


Fig. 10 Calculated and measured Nusselt number ratios;  $Ro = 0.0$ ,  $\Delta\rho/p = 0.115$

**Spanwise-Averaged and Regional-Averaged Heat Transfer Coefficients and Comparison With Experimental Data.**

Comparisons were made with the experimental data of Azad et al. [9] in order to provide a thorough evaluation of the present second moment closure model. Figures 10 through 12 are plots of the spanwise-averaged and regional-averaged Nusselt number ratios ( $Nu/Nu_0$ ) for each of the three cases ( $Ro=0.0$ ,  $Ro=0.11$  ( $\beta = 90$  deg), and  $Ro=0.11$  ( $\beta = 135$  deg)). The Reynolds number and the inlet coolant-to-wall density ratio were held constant at values of 10,000, and 0.115, respectively. Note that the experimental regional-averaged Nusselt number in Azad et al. [9] is based on the projected area of each copper plate rather than the true heat transfer surface area which includes the 45-deg rib-increased area. However, the predicted regional-averaged Nusselt

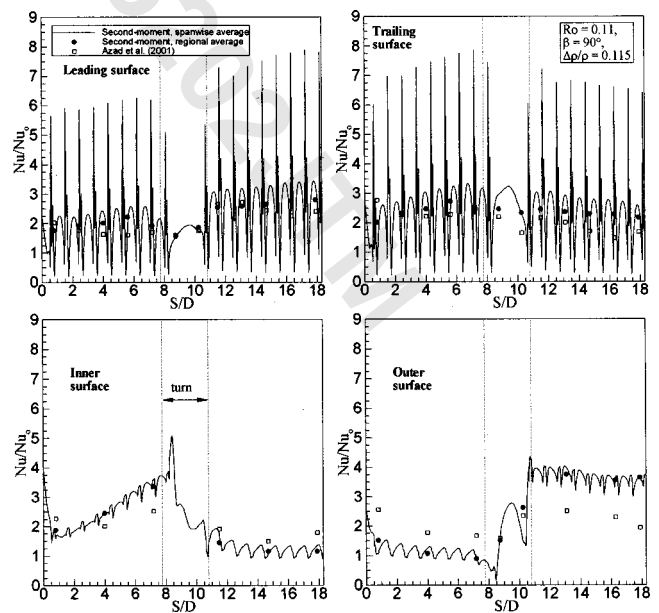
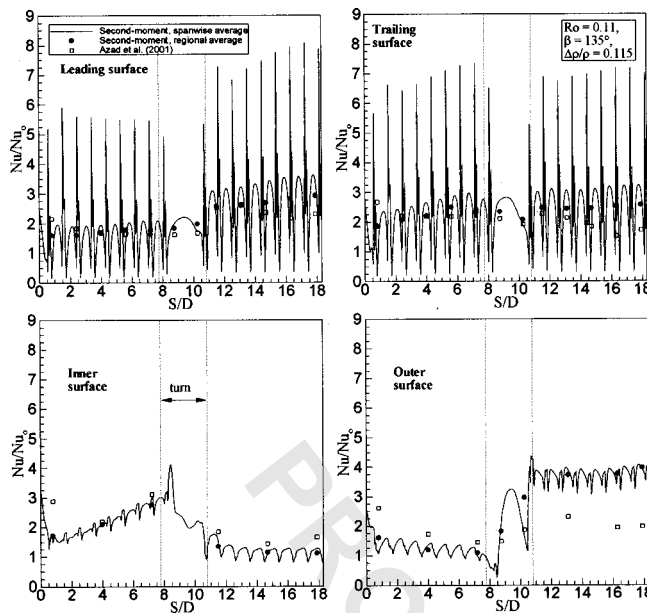


Fig. 11 Calculated and measured Nusselt number ratios;  $Ro = 0.11$ ,  $\beta = 90$  deg  $\Delta\rho/p = 0.115$



**Fig. 12** Calculated and measured Nusselt number ratios;  $Ro = 0.11$ ,  $\beta = 135$  deg  $\Delta\rho/\rho = 0.115$

number is based on the true heat transfer area for the test surfaces with 45-deg ribs which is 1.25 times the projected area. Therefore, the experimental data were divided by 1.25 to reasonably compare with our regional-averaged Nusselt number, except for the inner and outer surfaces where there were no ribs.

In Fig. 10 (case 1), the spanwise-averaged Nusselt number distributions on the leading and trailing surfaces show periodic spikes. The higher spikes are caused by the flow impingement on the ribs, and the lower spikes are caused by the flow reattachment between the ribs. The Nusselt number ratios are lower just upstream and downstream of the ribs and higher in the regions between the ribs. The Nusselt number ratios increase until about the midsection between the seventh and eighth rib, which is similar to Jang's et al. [26] 45-deg-rib case in a square channel. This phenomenon is caused by the rib-induced secondary flow becoming stronger along the duct as discussed in Fig. 4 and also mentioned by Han and Park [1]. The Nusselt number distribution on the inner surface shows that (in the first passage) it increases all the way to rib 9 as a result of the secondary flow that pushes the cold fluid towards the inner surface. As was shown in Fig. 4, the direction of the secondary flow in the turn is reversed becoming from inner to outer surface, which results in sharp decrease of the Nusselt number on the inner wall. In the second passage, the Nusselt number values at the inner surface are low due to hot fluid coming from the outer and ribbed surfaces. For the same reasons discussed above, the Nusselt number distribution on the outer surface is the opposite of the Nusselt number distribution on the inner surface.

Figure 11 (case 2:  $Ro=0.11$ ,  $\beta=90$  deg) shows that the heat transfer coefficients on the leading surface decreased approximately 8 percent in the first passage when compared to the stationary case, while increased approximately 14 percent in the second passage. The decrease and increase in heat transfer coefficients were due to the Coriolis force. On the trailing surface, the heat transfer increased approximately 12 percent in the first passage as compared to the stationary case while decreased by 5 percent in the rest of the second passage.

Figure 12 ( $Ro=0.11$ ,  $\beta=135$  deg) shows that the heat transfer coefficients on the leading surface decreased approximately 22 percent in the first passage when compared to the stationary case, while increased approximately 16 percent in the second passage. On the trailing surface, the heat transfer increased approximately 3 percent (in the first passage) and 7 percent (in the second pas-

sage) when compared to the stationary case. The reason why the Nusselt number ratios in case 3 ( $\beta=135$  deg) decreased more in the first pass leading and trailing sides and increased more in the second pass leading and trailing sides compared to case 2 ( $\beta=90$  deg) can be understood in light of the conceptual secondary flow diagram in Fig. 2.

The rotation-induced vortices in the 135-deg configuration move along the full face of the leading or trailing surfaces. However, the rotation induced vortices in the 90-deg configuration move along only one-half the face of the leading or trailing surfaces. With this in mind, we notice in Fig. 2 that the two secondary flows produced by rotation and angled ribs for the rotating 135-deg duct combine in the first passage to destructively (opposite direction) reduce heat transfer on both the leading surface (a 22-percent decrease compared to an 8 percent decrease in  $\beta=90$  deg) and the trailing surface (a 3-percent increase compared to a 12 percent increase in  $\beta=90$  deg). Moreover, they combine in the second passage to constructively (same direction) enhance heat transfer on both the leading surface (a 16-percent increase compared to a 14-percent increase in  $\beta=90$  deg) and the trailing surface (a 7-percent increase compared to a 5-percent decrease in  $\beta=90$  deg). On the other hand, the two secondary flows produced by rotation and angled ribs for the rotating 90-deg duct combine to (i) constructively (same direction) enhance heat transfer for only one half of each of the leading and trailing surfaces, and (ii) destructively (opposite direction) reduce heat transfer for the other half of each of the leading and trailing surfaces. The overall predicted Nusselt number behavior was relatively close to Azad et al. [9] data. However, the predicted Nusselt numbers on the outer surface and part of the trailing surface for the second-pass of the rotating case were over-predicted. This may be partly attributed to the fact that the predicted Nusselt number ratios are based on a uniform wall temperature boundary condition, while the experimental ones are based on a uniform wall heat flux boundary condition.

This computational study can be used to visualize the rib-induced, turn induced, and rotation induced secondary flows in the two-pass rectangular channels for both 90 and 135-deg orientations. This will help in designing better coolant passages which save coolant flow consumption and improve turbine efficiency. Moreover, this study reveals that the 135-deg orientation has a lower Nusselt number in the first pass leading and trailing sides compared to the 90-deg orientation. This should be taken into consideration by the internal cooling designer to prevent excessive heating should the design is based only on the 90-deg orientation assumptions.

## Conclusions

A validated multi-block RANS method was employed to predict three-dimensional flow and heat transfer in a rotating two-pass rectangular channel ( $AR=2:1$ ) roughened with 45-deg angled ribs on both the leading and trailing sides. Two channel orientations are studied:  $\beta=90$  and 135-deg. The present near-wall second-moment closure model results were compared with the experimental data of Azad et al. [9]. It predicted fairly well the complex three-dimensional flow and heat transfer characteristics resulting from the angled ribs, sharp 180-deg turn, rotation, centrifugal buoyancy forces and channel orientation. The inclined ribs start two counter-rotating vortices that oscillate in size along the streamwise direction. For case 1, the secondary flow results in steep temperature gradients and high heat transfer coefficients on both the inner and ribbed surfaces (for the first passage) and on both the outer and ribbed surfaces (for the second passage). In the turn, the two counter-rotating vortices convect fluid from the core towards the outer surface, resulting in higher heat transfer coefficients on the outer surface. For case 2 ( $\beta=90$  deg), rotation-induced cross-stream secondary flow distorts the rib induced vortices and consequently, rotation shifts the temperature contours and affects the heat transfer coefficients from both the leading and

trailing surfaces. For case 3 ( $\beta = 135$  deg), rotation-induced cross-stream secondary flow distorts the rib induced vortices. The rotation induced vortices have more space (compared to case 2) either to combine constructively (same direction) or destructively (opposite direction) with the rib induced vortices and thus produce greater increase or decrease in the heat transfer coefficients.

## Acknowledgments

The leading author, Mohammad Al-Qahtani, received a fellowship from King Fahd University; Saudi Arabia, for his Ph.D. study at Texas A&M University. This work was supported by the Texas Higher Education Coordination Board—Advanced Technology Program under grant number 999903-165. The computations were performed on the Cray J90 at the Texas A&M Supercomputer Center under a supercomputer research grant. The GRIDGEN software was supported by Pointwise Inc. The support of all of the above institutions is greatly appreciated.

## Nomenclature

- $D_h, D$  = hydraulic diameter, m  
 $e$  = rib height, m  
 $h$  = heat transfer coefficient,  $W/m^2 \cdot K$   
 $k$  = thermal conductivity of coolant,  $W/m \cdot K$   
 $Nu$  = local Nusselt number,  $hD/k$   
 $Nu_o$  = Nusselt number in fully developed turbulent nonrotating tube flow,  $hD/k$   
 $Pr$  = Prandtl number  
 $Re$  = Reynolds number,  $\rho W_b D_h / \mu$   
 $r_i$  = inner radius of bend, m  
 $Ro$  = rotation number,  $\Omega D_h / W_b$   
 $R_r$  = radius from axis of rotation, m  
 $S$  = streamwise distance, m  
 $T$  = local coolant temperature, SDC  
 $T_o$  = coolant temperature at inlet,  $^{\circ}C$   
 $T_w$  = wall temperature,  $^{\circ}C$   
 $W_b$  = bulk velocity in streamwise direction, m/s  
 $\alpha$  = rib angle  
 $\beta$  = angle of channel orientation measured from direction of rotation  
 $\rho$  = density of coolant,  $kg/m^3$   
 $\Delta\rho/\rho$  = inlet coolant-to-wall density ratio [based on ideal gas assumption],  $(T_w - T_o)/(T_w - T_o)$   
 $\Omega$  = rotational speed, rad/s  
 $\theta$  = dimensionless temperature,  $(T - T_o)/(T_w - T_o)$   
 $\mu$  = dynamic viscosity of coolant,  $N \cdot s/m^2$

## References

- Han, J. C., and Park, J. S., 1988, "Developing Heat Transfer in Rectangular Channel with Rib Turbulators," *Int. J. Heat Mass Transf.*, **31**, No. 1, pp. 183–195.
- Ekkad, S. V., and Han, J. C., 1997, "Detailed Heat Transfer Distributions in Two-pass square Channels with Rib Turbulators," *Int. J. Heat Mass Transf.*, **40**, No. 11, pp. 2525–2537.
- Wagner, J. H., Johnson, B. V., Graziani, R. A., and Yeh, F. C., 1992, "Heat Transfer in Rotating Serpentine Passages with Trips Normal to the Flow," *ASME J. Turbomach.*, **114**, pp. 847–857.
- Johnson, B. V., Wagner, J. H., Steuber, G. D., and Yeh, F. C., 1994, "Heat Transfer in Rotating serpentine Passage with Trips Skewed to the Flow," *ASME J. Turbomach.*, **116**, pp. 113–123.
- Johnson, B. V., Wagner, J. H., Steuber, G. D., and Yeh, F. C., 1994, "Heat Transfer in Rotating serpentine Passage with selected Model Orientations for Smooth or Skewed Trip Walls," *ASME J. Turbomach.*, **116**, pp. 738–744.
- Parsons, J. A., Han, J. C., and Zhang, Y. M., 1995, "Effects of Model Orientation and Wall Heating Condition on Local Heat Transfer in a Rotating Two-Pass Square Channel with Rib Turbulators," *Int. J. Heat Mass Transf.*, **38**, No. 7, pp. 1151–1159.
- Zhang, Y. M., Han, J. C., Parsons, J. A., and Lee, C. P., 1995, "Surface Heating Effect on Local Heat Transfer in a Rotating Two-pass Square Channel With 60 deg Angled Rib Turbulators," *ASME J. Turbomach.*, **177**, pp. 272–280.
- Zhang, S., and Han, J. C., 1996, "Local Heat Transfer in Rotating Smooth and Ribbed Two-Pass Square Channels with Three Channel Orientations," *ASME J. Heat Transfer*, **118**, pp. 578–584.
- Azad, GM S., Uddin, M. J., Han, J. C., Moon, H. K., and Glezer, B., 2001, "Heat Transfer in Two-Pass Rectangular Rotating Channels with 45 deg Parallel and Crossed Rib Turbulators," submitted to the 2001 IGTI Conference to be held in New Orleans, LA.
- Liou, T. M., Hwang, J. J., and Chen, S. H., 1993, "Simulation and Measurement of Enhanced Turbulent Heat Transfer in a Channel With Periodic Ribs on One Principal Wall," *Int. J. Heat Mass Transf.*, **36**, pp. 507–517.
- Stephens, M. A., Shih, T. I-P., and Civinskas, K. C., 1995, "Computation of Flow and Heat Transfer in a Rectangular Channel with Ribs," *AIAA Paper 95-0180*.
- Rigby, D. L., Steinhilsson, E., and Ameri, A. A., 1997, "Numerical Prediction of Heat Transfer in a Channel with Ribs and Bleed," *ASME Paper 97-GT-431*.
- Stephens, M. A., Chyu, M. K., and Shih, T. I-P., 1996, "Computation of Convective Heat Transfer in a Square Duct with Inclined Ribs of Rounded Cross Section," *ASME Paper 96-WA/HT-12*.
- Stephens, M. A., and Shih T. I-P., 1997, "Computation of Compressible Flow and Heat Transfer in a Rotating Duct With Inclined Ribs a 180 deg Bend," *ASME Paper 97-GT-192*.
- Shih, T. I-P., Lin, Y.-L., Stephens, M. A., and Chyu, M. K., 1998, "Flow and Heat Transfer in a Ribbed U-Duct under Typical Engine Conditions," *ASME Paper 98-GT-213*.
- Prakash, C., and Zerkle, R., 1995, "Prediction of Turbulent Flow and Heat Transfer in a Ribbed Rectangular Duct With and Without Rotation," *ASME J. Turbomach.*, **177**, pp. 255–264.
- Bonhoff, B., Tomm, U., Johnson, B. V., and Jennions, I., 1997, "Heat Transfer Predictions For Rotating U-Shaped Coolant Channels With Skewed Ribs and with Smooth Walls," *ASME 97-GT-162*.
- Iacovides, H., 1998, "Computation of Flow and Heat Transfer Through Rotating Ribbed Passage," *Int. J. Heat Fluid Flow*, **19**, pp. 393–400.
- Rigby, D. L., 1998, "Prediction of Heat and Mass Transfer in a Rotating Ribbed Coolant Passage with a 180 Degree Turn," *ASME Paper 98-GT-329*.
- Iacovides, H., and Raisee, M., 1999, "Recent Progress in the Computation of Flow and Heat Transfer in Internal Cooling Passages of Turbine Blades," *Int. J. Heat Fluid Flow*, **20**, pp. 320–328.
- Chen, H. C., Jang, Y. J., and Han, J. C., 2000, "Computation of heat transfer in rotating two-pass square channels by a second-moment closure model," *Int. J. Heat Mass Transf.*, **43**, No. 9, May, pp. 1603–1616.
- Chen, H. C., Jang, Y. J., and Han, J. C., 2000, "Near-Wall Second-Moment Closure for Rotating Multi-pass Cooling Channels," *Int. J. Heat Mass Transf.*, **14**, No. 2, pp. 201–209.
- Wagner, J. H., Johnson, B. V., and Kopper, F. C., 1991, "Heat transfer in Rotating Serpentine Passage with Smooth Walls," *ASME J. Turbomach.*, **113**, pp. 321–330.
- Jang, Y. J., Chen, H. C., and Han, J. C., 2000, "Computation of Flow and Heat Transfer in Two-Pass Channels with 60° Ribs," *AIAA Paper 2000-1036*, 38th Aerospace Science Meeting & Exhibit, Reno, NV, January 10–13.
- Jang, Y. J., Chen, H. C., and Han, J. C., 2000, "Numerical Prediction of the Flow and Heat Transfer in a Two-Pass Square Duct with 90° Ribs," 8th International Symposium on Transport Phenomena and Dynamics of Rotating Machinery (ISROMAC-8), Honolulu, HI, March 26–30, **1**, pp. 580–587.
- Jang, Y. J., Chen, H. C., and Han, J. C., 2000, "Flow and Heat Transfer in a Rotating Square Channel with 45° Angled Ribs by Reynolds Stress Turbulence Model," *ASME 2000-GT-0229*.
- Rohsenow, W. M., and Choi, H., 1961, *Heat, Mass and Momentum Transfer*, Prentice-Hall Englewood Cliffs, NJ.